Dynamic induced softening in frictional granular materials investigated by discrete-element-method simulation

Laure Lemrich, Jan Carmeliet, Paul A. Johnson, Robert Guyer, and Xiaoping Jia

Phys. Rev. E **96**, 062901 — Published 1 December 2017

DOI: 10.1103/PhysRevE.96.062901

Dynamic induced softening in frictional granular material investigated by DEM simulation

Laure Lemrich* and Jan Carmeliet
Chair of Building Physics, ETHZ, Wolfgang-Paulistrasse 15, CH-8093 Zurich, Switzerland
Laboratory of Multiscale Studies in Building Physics, Empa, Überlandstrasse 129, CH-8600 Dübendorf, Switzerland

Paul A. Johnson
Solid Earth Geophysics Group, Los Alamos National Laboratory, MS D443, Los Alamos, 87545 New Mexico, USA

Robert Guyer
Solid Earth Geophysics Group, Los Alamos National Laboratory, MS D443, Los Alamos, 87545 New Mexico, USA
Department of Physics, University of Nevada, Reno (NV), USA

Xiaoping Jia
Institut Langevin, ESPCI Paris, CNRS UMR 7587 - 1 rue Jussieu, 75005 Paris, France
(Dated: November 16, 2017)

A granular system composed of frictional glass beads is simulated using the Discrete Element Method. The inter-grain forces are based on the Hertz contact law in the normal direction with frictional tangential force. The damping due to collision is also accounted for. Systems are loaded at various stresses and their quasi-static elastic moduli are characterized. Each system is subjected to an extensive dynamic testing protocol by measuring the resonant response to a broad range of AC drive amplitudes and frequencies via a set of diagnostic strains. The system, linear at small AC drive amplitudes has resonance frequencies that shift downward (i.e., modulus softening) with increased AC drive amplitude. Detailed testing shows that the slipping contact ratio does not contribute significantly to this dynamic modulus softening, but the coordination number is strongly correlated to this reduction. This suggests that the softening arises from the extended structural change via break and remake of contacts during the rearrangement of bead positions driven by the AC amplitude.

INTRODUCTION

Granular materials are comprised of an ensemble of randomly packed solid particles and the mechanical behaviour of the systems is basically determined by the interactions at contacts. These materials are ubiquitous in industry and in geosciences, and are also of fundamental interest to ground motion and earthquake dynamics. Unlike ordinary materials, granular media can exhibit solid-like and fluid-like behaviour and there exists transition between the two states [1]. A granular solid shows strong nonlinear elasticity and sound propagation provides a footprint of this feature [2–5]. The nonlinear dynamic response found in granular media such as resonance frequency softening, slow dynamics and harmonic generation [6–9] is very similar to those discovered in rocks [10–14].

Other nonlinear behavior observed in granular solids include stress- strain hysteresis [13], fabric anisotropy [15, 16] and loading-history- dependent sound velocity [6, 15, 16]. Such behaviour is closely related to the fragility of the granular solid determined by the very inhomogeneous and anisotropic contact network ; it may react elastically to load changes in one specific direction but infinitesimal loads in another direction will drive rearrangements in the sample [17].

If the jammed granular solids are treated as homogenous, for example by coarse graining [18], the effective medium theory (EMT) [19–21] may be applied using an affine approximation to qualitatively connect the global response, like the bulk and shear elastic moduli K and G, to the local geometry. In the case of isotropic compression, the EMT based on the Hertz contact law predicts the scaling for $K \propto (\phi Z_c)^{2/3}\sigma^{1/3}$ and $G \propto (\phi Z_c)^{2/3}\sigma^{1/3}$ where σ is the confining pressure, ϕ the packing fraction and Z_c the coordination number (assumed to be constant)[5, 19, 20]. The scaling of K and G can be determined by the velocities of compression and shear waves, via $v_P = [(K + 2G)/\rho]^{1/2}$ and $v_S = (G/\rho)^{1/2}$ where $\rho = \rho_0\phi$ and ρ_0 are respectively the packing and the particle densities [5, 19]. It has been revealed by numerical simulations that at low σ the bulk modulus still scales as $K \propto \sigma^{1/3}$ while the shear modulus scales as $G \propto \sigma^{2/3}$ near unjamming [5, 24]. This observation can be explained by the breakdown of the effective medium theory due to the nonaffine motion caused by the rearrangement of the contact network or particle positions.

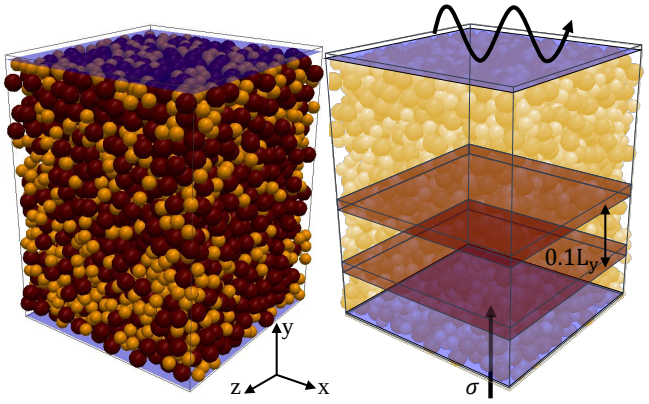

FIG. 1. (left) Representation of a sample, with large particles in a darker color. The packing is enclosed between two walls along the y-direction. (right) The two horizontal sections in the sample enclose a local region where wall effects are minimal. The perturbation are movements of the top wall while the bottom wall adjusts to maintain constant loading stress.

Current numerical works on vibrational properties focus on the density of modes as the packing fraction decreases to the jamming point [22–28]. An issue of broad interest is the evolution of material characteristics as a granular packing approaches the unjamming transition by vibration-induced fluidization [29]. The combination of acoustic probing and pumping in the nonlinear regime allows us to highlight the material softening near this transition, using sound velocity [9, 30] or resonance [7] measurements. Simulations with 2D disk packings using a normal Hertzian contact force and a tangential viscous force have qualitatively reproduced the experimental observation of resonance frequency softening with increasing dynamic amplitude. This behaviour arises from rearrangements of the contact network, resulting in a reduction in the average contact number but without significant rearrangement of particle positions [28]. However, the effect of friction on the elastic softening [9, 30] is absent in these frictionless systems.

Here we address this issue by simulating the effects of resonance frequency softening in confined 3D frictional bead packings under an applied dynamic (AC) drive. We drive the confined granular packing at larger and larger amplitudes to explore the nonlinear response of the material that provide clues to the transition from a solid state to a fluid state where the mobility of particles becomes important, nevertheless having a mean-square displacement smaller than the particle size. Note that the granular packing does not flow in our simulations due to the absence of macroscopic shear, but merely approaches the fluid state with significant elastic softening and particle position rearrangement [9, 29]. In the next section, we present the numerical model and the protocol of tests and then we show the simulation results. All these findings will be analysed using the mean- field approach.

NUMERICAL MODEL AND METHODOLOGY

We apply the Discrete Element Method [31] (LIGGGHTS 3.4 [32]) to simulate the mechanical behavior of 3D glass bead packings under static and oscillatory loading stress. The Hertz contact law is used to reproduce normal elastic interactions between elastic spheres and an elastofrictional model is implemented to describe the tangential interaction. The collision process is also included for the viscoelastic damping.

Intergrain forces

The total force $\boldsymbol{F}_i$ acting on a particle i is the sum of the contact forces with interacting particles $j \in J$ and viscosity damping. Specifically, it is the sum of a normal force $\boldsymbol{F}_n$ based on the Hertz theory, and a tangential force $\boldsymbol{F}_t$ based on an approximation of the Mindlin model [33]:

$$\begin{aligned}\boldsymbol{F}_i = &\sum_{j\in J}\left(k_n\delta n_{ij}^{3/2}\hat{\boldsymbol{n}}_{ij} - \gamma_n \boldsymbol{v}_{ij}\hat{\boldsymbol{n}}_{ij}\right)\\ &-\sum_{j\in J}\left(k_t\delta n_{ij}^{1/2}\delta t_{ij}\hat{\boldsymbol{t}}_{ij} - \gamma_t \boldsymbol{v}_{ij}\hat{\boldsymbol{t}}_{ij}\right) - \gamma_a \boldsymbol{v}_i\end{aligned} \tag{1}$$

where δn_{ij} and δt_{ij} are the normal overlap and relative tangential displacement between particles i and j. δt_{ij} is truncated to fulfil $\|\boldsymbol{f}_t\| < \mu_s\|\boldsymbol{f}_n\|$ where μ_s is the coefficient of the Coulomb friction, $\boldsymbol{f}_n$ is the normal force at one contact and $\boldsymbol{f}_t$ is the tangential force. Particles over threshold are modelled as slipping against each other. $\hat{\boldsymbol{n}}_{ij}$ and $\hat{\boldsymbol{t}}_{ij}$ are the normal and tangential unit vectors of each contact ij. Finally, $\boldsymbol{v}_i$ is the velocity of particle i while $\boldsymbol{v}_{ij} = \boldsymbol{v}_j - \boldsymbol{v}_i$. γ_a is the viscous damping coefficient for numerical stabilisation.

Provided with the Young's modulus Y_g, shear modulus G_g and loss coefficient β_g of the grains, the normal and tangential elastic constants are:

$$k_n = \frac{4}{3}Y_g\sqrt{R^*} \tag{2}$$

$$k_t = 8G_g\sqrt{R^*} \tag{3}$$

and the viscoelastic parameters related to collision losses:

$$\gamma_n = 2\beta_g(R^*\delta n_{ij})^{1/4}\sqrt{\frac{5}{3}m^*Y_g} \tag{4}$$

$$\gamma_t = 4\beta_g(R^*\delta n_{ij})^{1/4}\sqrt{\frac{10}{6}m^*G_g} \tag{5}$$

The effective radius R^* and mass m^* depend on the respective radii R and masses m of the two particles: $1/R^* = 1/R_i + 1/R_j$ and $1/m^* = 1/m_i + 1/m_j$.

The equation governing rotational velocity is:

$$I_i\frac{d\boldsymbol{\Omega}_i}{dt} = \boldsymbol{r}_i \times \boldsymbol{F}_{t,i} + \boldsymbol{T}_{i,j} \tag{6}$$

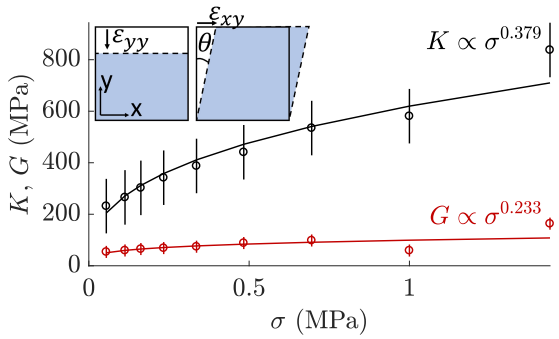

FIG. 2. Elastic and shear moduli K and G of the granular samples as a function of loading stress σ. power-law The inset shows the compression and shear protocols.

with I_i the moment of inertia, $\boldsymbol{r}_i$ the vector from the center of the particle i to the contact point, $\boldsymbol{F}_{t,i}$ the tangential component of the force exerted on the particle i and a torque at each contact:

$$\boldsymbol{T}_{i,j} = \mu_r k_n \delta n_{ij} R_i \frac{\boldsymbol{\Delta\Omega}_{ij}}{\|\boldsymbol{\Delta\omega}_{ij}\|} \tag{7}$$

with μ_r the rolling resistance and $\boldsymbol{\Delta\Omega}_{ij} = (R_i\boldsymbol{\Omega}_i + R_j\boldsymbol{\Omega}_j)/(R_i + R_j)$ is the relative angular velocity [34].

Energy is basically dissipated via frictional damping in sliding and, in collisonal interactions, via the coefficient $\beta = ln(e)/\sqrt{ln^2(e) + \pi^2}$, with e the restitution coefficient.

Granular sample preparation

3D samples are created by randomly filling particles of radius r_1 or r_2 into a box with dimensions $(l_x, l_y^{init}, l_z) = (10^{-2}, 2.5 \times 10^{-2}, 10^{-2})$ m (See Fig. 1). Particles have a density $\rho_0 = 2500\text{kg/m}^3$. The y-axis is vertical (with $y = 0$ at the bottom) and periodic boundary conditions are applied in the x- and z-directions. Two walls enclose the system in y-direction. These walls can be moved via a fixed function or servo-controlled, in which case an algorithm will move the wall with a maximal velocity v_{max} to maintain a constant loading stress.

A variable velocity from $v_{max} = 6$ m/s to 0 is applied to the bottom of the box to compact the particles while the top wall moves to reach a static loading stress σ. After a period $\Delta t_1 = 0.2$ s, the bottom wall moves with a sinusoidal vertical movement $A\sin(\omega t)$ with $\omega = 1.26 \times 10^5$ rad/s for a period $\Delta t_2 = 2$ s to perturb the system and bring it closer to equilibrium. The amplitude of perturbation $A = l_y 5 \times 10^{-5}$ with l_y the sample height when perturbation starts. Preliminary simulations showed that this value drives rearrangements and compaction in the samples. Finally the bottom wall is stopped and the packing is allowed to evolve and relax during period $\Delta t_3 = 7.8$ s, to reach a sample height of $l_y \approx 1.2 \times 10^{-2}$ m with about 4100 particles. Granular samples are confined by the loading stress σ, set at 10 logarithmically spaced values between $\sigma = 10$ kPa and $\sigma = 1438$ kPa. The resulting static strain ε_0 is estimated as $\sim 10^{-4} - 10^{-3}$ with a limited precision at low values depending on the test protocol.

All simulations are run with $\gamma_a = 10^{-7}$ kg/s (air effect at room temperature) and timestep $dt = 8 \times 10^{-8}$ s. Particles have contact force parameters: $Y_g = 65$ GPa, $\nu_g = 0.25$, $K_g = 43.33$ GPa, $G_g = 26$ GPa, $\mu_s = 0.22$, $\beta_g = 0.0163$ and $\mu_r = 0.01$. The radii of particles are $r_1 = 3 \times 10^{-4}$ m and $r_2 = 4 \times 10^{-4}$ m. 60% of the sample mass is made of particles with radius r_1 and 40% with radius r_2.

Tests under quasistatic compression and shear

The granular samples are compressed by uniaxial load or sheared at constant volume to determine their bulk and shear moduli, respectively (see figure 2, inset). The driving incremental strains (cycle) are $\Delta\varepsilon \sim \times 10^{-6}$.

During a compression test, the bottom wall remains fixed while the top wall moves downward at constant velocity v_{lid} to make a small cycle around the confining stress σ. The top wall first moves down at velocity v_{lid} over a period Δt_{compr}, then up at v_{lid} for $2\Delta t_{compr}$, then back down at v_{lid} for Δt_{compr}. The compressive strain $\varepsilon_{yy} = (l_y - l_y^0)/l_y^0$ (the deviation of sample height l_y from its initial value l_y^0) and compressive stress σ_{yy} on the top wall are recorded. The stress for an isotropic packing is given as:

$$\sigma_{yy} = \frac{3Y(1-\nu)}{(1+\nu)}\varepsilon_{yy} \tag{8}$$

with Young's Modulus Y and Poisson ratio ν of the granular medium.

A shear test is performed by imposing the wall at fixed positions along the y-axis, while the top wall is sheared along the x-axis. The wall moves at velocity v_{lid} in the x-direction for a time Δt_{compr}, then moves back at v_{lid} for $2\Delta t_{compr}$, and finally at v_{lid} for Δt_{compr}. The shear stress σ_{yx} and the strain $\varepsilon_{yx} = (x_{lid} - x_{lid}^0)/l_y^0$ are recorded during the simulation. Assuming isotropic linear elastic behavior, the stress-strain relation is given as:

$$\sigma_{yx} = 2G\varepsilon_{yx} \tag{9}$$

Equations (8) and (9) constitute a system of two equations with two unknowns: the Young's Modulus Y and Poisson ratio ν of the granular material. The bulk and shear moduli are given by $K = Y/3(1-2\nu)$ and $G = Y/2(1+\nu)$. The moduli were determined using the full cycle, with negligible hysteresis observed during the loading-unloading.

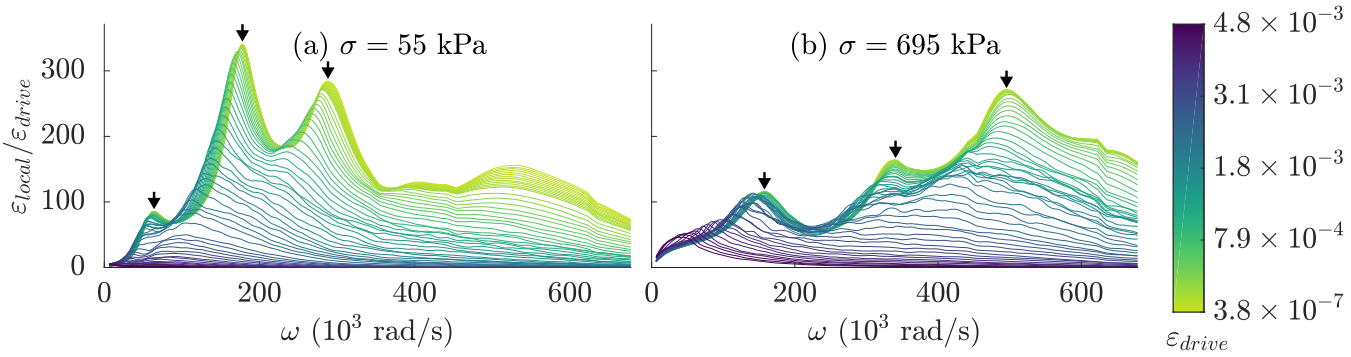

FIG. 3. Two series of frequencies sweeps obtained for $\sigma = 55$ kPa (a) and $\sigma = 695$ kPa. Line color represents the drive strain of each sweep (from $\varepsilon_{drive} = 3.8 \times 10^{-7}$ in light green to $\varepsilon_{drive} = 4.8 \times 10^{-3}$ in dark blue). Harmonics are visible. Resonant frequencies decrease and peak broaden as drive strain increase. As shown in Fig. 5, each figure correspond to a different boundary condition.

Compression and shear tests were both performed at a velocity $v_{lid} = 10^{-7}$ m/s for $\Delta t_{compr} = 0.2$ s. The highest velocity ensuring quasi-static measurements is computed for $I = 2\dot{\gamma} r_{min}/\sqrt{\sigma_{min}/\rho} < 10^{-3}$, with $r_{min} = 3 \times 10^{-4}$ m, $\sigma_{min} = 10$ kPa, $\rho \approx 1400$ kg/m^3. The strain rate $\dot{\gamma} = v_{lid}/l_y$ implies $v_{lid} < 5.79 \times 10^{-2}$ m/s for our samples.

Tests under compressional vibration

A probing layer inside the sample with y-coordinate comprised between $0.2l_y$ and $0.4l_y$ has been selected (to avoid the wall effect) to study the dynamic strain of the granular packing ε_{local} to an applied vibration. The system is driven for $N(= 100)$ periods at each drive frequency so that it reaches quasi-steady state and data are averaged over the last $N' = 60$ periods and recorded. Measurements are made 50 times per period.

Frequency sweeps are performed in the granular packings under different confining stress σ, maintained by the bottom wall. The applied vibration is introduced by vertically moving the top wall with $A_{drive}\sin(\omega t)$ for N periods. The frequency during sweeps is increased from $\omega = 6.2 \times 10^3$ rad/s to $\omega = 6.2 \times 10^5$ rad/s by steps of 1.9×10^2 rad/s. The drive amplitude A ranges from 5×10^{-8} to 6×10^{-5} m. The dynamic strain is computed as the amplitude A_{drive} divided by the average height of the system $\langle l_y \rangle$: $\varepsilon_{drive} = A_{drive}/\langle l_y \rangle$,varying accordingly from 4.13×10^{-6} to 4.95×10^{-3})

For measuring the resonance response of the sample, we investigate the dynamic strain of a local layer away from the nodes of the standing waves. Here, the local strain ε_{local} is computed as follows. First the instantaneous strain is determined as the relative difference between the local layer height $l(t)$ and its average l_{ω_i} over the last $N' = 60$ periods of the system driven at ω_i:

$$\varepsilon_{\omega_i}(t) = \frac{l(t) - l_{\omega_i}}{l_{\omega_i}} \tag{10}$$

The strain $\varepsilon_{\omega_i}(t)$ is composed of a slowly- evolving component due to the relaxation of the specimen and a component oscillating at drive frequency. We remove the slowly-evolving component by subtracting a moving-average window with a length equivalent to one period of the system. Finally we fit the amplitude and phase of the sinus $\varepsilon_{local} sin(\omega t + \phi)$ on the remaining strain oscillation.

Slipping contact ratio and coordination number

In addition to the dynamic strain, we also studies the Slipping Contact Ratio $SCR(t)$ of the probe layer which is the ratio between contacts 'slipping' in regard to each other (algorithmically when the Coulomb threshold is applied to the tangential force) to all contacts in the probing layer. The average $\langle SCR \rangle$ corresponding to a frequency ω_i is obtained over the last N' periods of $SCR(t)$ driven at ω_i. Similarly, the coordination number $Z_c(t)$ is the average number of contacts of particles in the probing layer. $\langle Z_c \rangle$ is the average of $Z_c(t)$ over the last N' periods. In this work, we investigate the values of ε_{local}, $\langle Z_c \rangle$ and $\langle SCR \rangle$ in the same probing layer as a function of the driving frequency ω.

RESULTS AND DISCUSSION

Elastic Moduli

Fig. 2 shows the bulk K and shear G moduli obtained by compression and shear tests in granular samples as a

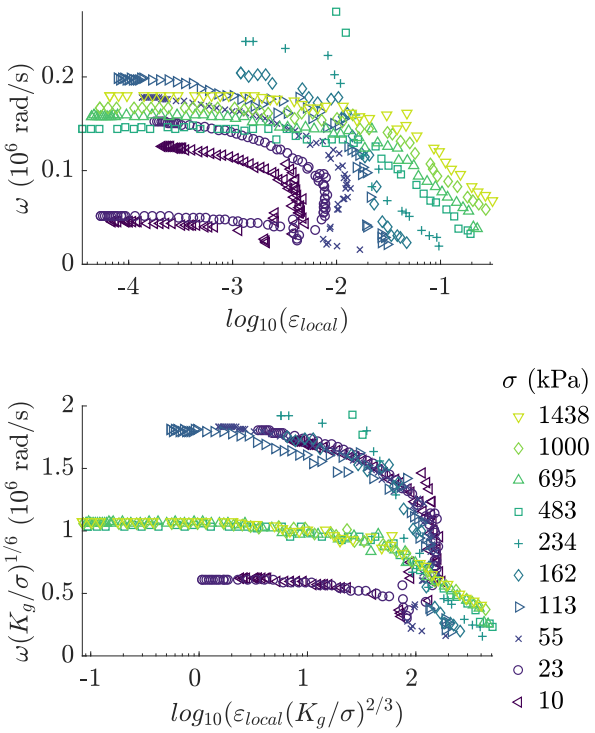

FIG. 4. The first modes are extracted from the frequency sweeps (Fig. 3 and reported in (a) as a function of local strain. When scaled according to predictions of Hertzian theory, resonances collapse onto primary curves (b). The two resonances correspond to different modes (Fig. 5). Resonant frequency remains constant for low drive strain, then decreases above a threshold value.

function of the confining stress σ. K scales as $\sigma^{0.379}$ being close to the Hertz theory prediction with a dependency of $\sigma^{1/3}$ [20] whereas G scales as $\sigma^{0.233}$ with an exponent lower than those found in other simulations with imposed confining pressure [5, 22, 35]. As shown below, the value of bulk modulus found here are in good agreement with the compressional sound velocity deduced from our main resonance simulation. We also observe a strong dependence of the elastic modulus on the coordination number and packing fraction of the samples [35]. In the present samples, the coordination number ranges from 4.38 to 4.95, and the packing fraction from 0.60 to 0.62, in the range expected for an isotropic packing of frictional particles [36].

Resonance, Hertzian scaling and softening

Figure 3 shows two series of frequency sweeps performed for low $\sigma = 10$ kPa and high $\sigma = 695$ kPa, respectively. Both figures show the results for a series of drive strains from $\varepsilon_{drive} = 3.8\times10^{-7}$ to 4.8×10^{-3} (the highest

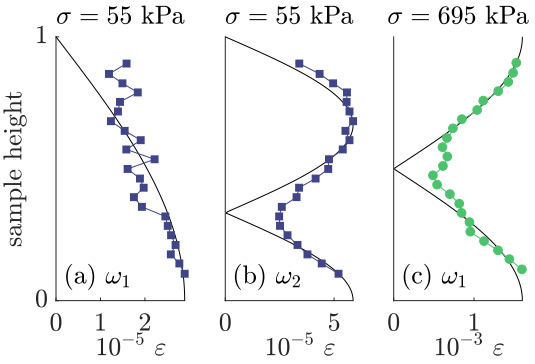

FIG. 5. Each figure shows the strain profile of the sample vibrated at resonance. The first and second modes (a) and (b) of a low stress sample show a closed boundary at the top and open at the bottom. In the high stress sample (c), both boundaries are open.

value for which a peak could be distinguished for all samples). At low drive strain, the resonance frequency does not decrease, but the system exhibits harmonics (shown with arrows on Fig. 3) as found in the experiments [8]. As the drive strain increases, resonance frequencies decrease and resonant peaks broaden and start to merge with each other.

We plot these frequency shifts in Fig. 4. The resonances ω satisfying $\omega < 2.5\times10^5$ rad/s are extracted detecting and fitting each peak with a third-order polynomial, and reported in Fig. 4(a). Samples at high loading stress, above 480 kPa show a clear linear regime at low local strain ε_{local} followed by a softening. This thresholding was selected because the two first modes at low loading stress merge as drive strain increases and, at high loading stress and high drive strain, only the first mode remains. The Hertz theory, as implemented in equation (1), predicts a contact force proportional to the overlap between two particles $f_n \propto \delta^{3/2}$. If our samples were to follow the mean-field approach based on the Hertzian contact, the resonance ω would scale as $\sigma^{1/6}$ [2] and the strain ε as $\sigma^{2/3}$ [20]. We apply this scaling and report the data on Fig. 4(b), where we observe that resonances collapse onto primary curves: two for low stresses and one for high stresses.

We note that resonant modes at $\sigma = 55$ kPa and $\sigma = 695$ kPa represent different boundary conditions. Fig. 5(a,b) shows the local strain ε vertical profile in a sample at $\sigma = 55$ kPa vibrated at its first and second modes ω_1 and ω_2. The data shows an approximately free boundary condition at the top wall with very small strain or stress, and a clamped-like boundary at the bottom wall with finite strain or stress. The first modes of such a system are $\lambda/4$ and $3\lambda/4$ (black line on (a) and (b)). In contrast, the high loading stress samples $\sigma = 695$ kPa shows clamped-like boundary conditions at both ends where the

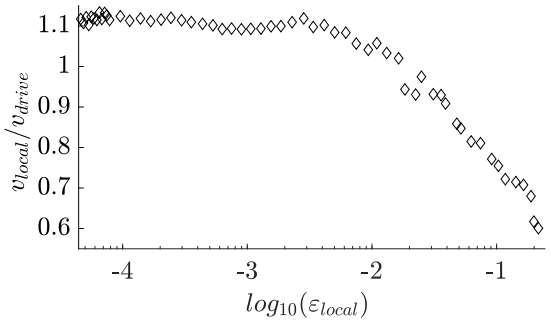

FIG. 6. Ratio of the average particle velocity v_{local} in the local layer to the maximal velocity of the wall v_{drive} under $\sigma = 695$ kPa. At low strain, the ratio of both velocities is roughly constant. At high strain, the local particle velocity decreases compared to drive velocity.

dynamic strain or stress is very small compared to the static strain or confining stress. The first mode, $\lambda/2$, and data are reported on Fig. 5(c). Data in all three cases follow the predicted modes. The deviation on the boundary and at the antinode are presumably due to the inherent fluctuation in the granular material. Fig. 4(b) thus shows a Hertzian scaling of the resonance for two different boundary conditions. At low loading stress, two modes are observed which soften at higher local strain, and merge together. Data for high loading stress supports higher local strains and shows a clear linear regime at low local strain. Moreover, from Figs. 4a and 5c, we measure a resonant frequency $\omega \sim 1.5 \times 10^5$rad/s with a wavelength $\lambda = 2l_y$ which gives a longitudinal sound speed $c = \lambda\omega/2\pi = 500$ m/s. The bulk modulus can then be deduced by $K = \rho c^2 \sim 625$ MPa, which is consistent with the value derived from the static compressional test (Fig. 2).

We also investigate the transmission of the kinetic energy into the granular system from the driving force, by comparing the average particle velocity v_{local} in the probing layer and the driving wall velocity v_{drive}. The particle velocity is obtained from the relation $E_{kin} = (1/2)M_g v_{local}^2$, with E_{kin} returned by simulations and the packing mass $M_g = 1.77 \times 10^{-3}$ kg for $\sigma = 695$ kPa. The maximal driving velocity of the wall is the product of the resonant frequency and the displacement amplitude: $v_{drive} = \omega A$. Fig. 6 shows that at low strain (linear regime) the ratio of the particle velocity to the driving is almost constant and equal to 1.1, but at higher strain it decreases to about 0.6. Furthermore we observe a striking similarity between this ratio and the resonance frequency decrease with increasing dynamic strain (Fig. 4(b) and Fig. 9(a)). This behaviour can be qualitatively understood in terms of the coefficient of amplitude transmission which depends on the acoustic impedance and accordingly the sound velocity of the granular sample [30]: the lower the sound velocity (due to elastic softening), the lower the transmission coefficient.

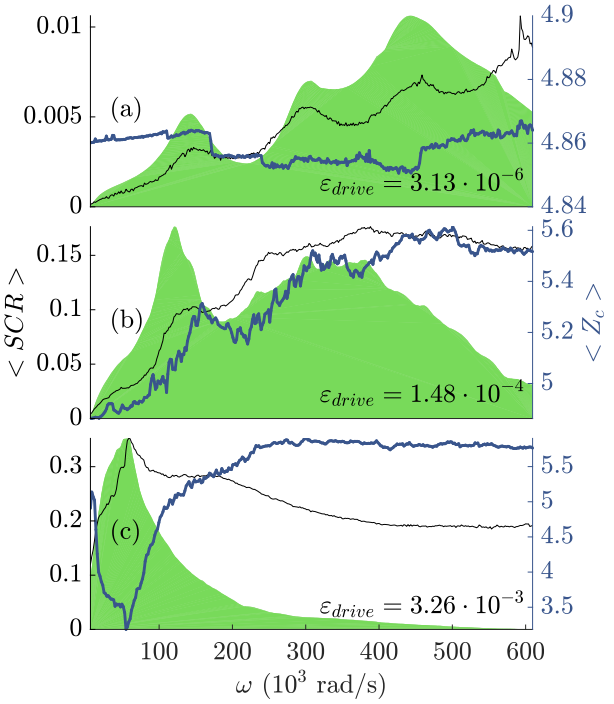

FIG. 7. Coordination number $\langle Z_c \rangle$ (right-hand vertical axis, thick line), Slipping Contact Ratio $\langle SCR \rangle$ (left-hand vertical axis, thin line) and normalized frequency spectrum (outlined in the background) in the linear (a), transition (b) and nonlinear (c) regions of the drive strain at loading stress $\sigma = 695$ kPa. Shifts in $\langle Z_c \rangle$ are below 0.01 for low drive strain. In the transition regime, Its average value increases as a result of perturbation up to a saturation value of 5.71. $\langle SCR \rangle$ increases peaks at resonant frequencies. In the nonlinear regime the system softens, and the coordination number decreases at resonance. Left axis shows the variation range for each case.

Changes of coordination number and slipping contact ratio upon applied vibration

To understand the responses of granular samples to the applied vibration, we investigate simultaneously the structural changes of the contact networks. More specifically, we study the coordination number and slipping contact ratio on the grain scale in our samples. Fig. 7 shows three frequency sweeps performed on a sample at $\sigma = 695$ kPa. The background outline represents a scaled profile of the frequency sweep. The percentage of slipping contacts $\langle SCR \rangle$ (left axis) is represented with a thin line while the average coordination number $\langle Z_c \rangle$ (right axis) is represented with a thick line. In the linear regime (a), the coordination number remains constant at ~ 4.86, with

variations due to small movements in the sample. The slipping contact ratio peaks at resonance, and progressively increases from 0 to 1% over the frequency sweep, showing a progressive mobilisation of contacts. At higher drive strain (b), the coordination number peaks around the first resonant mode and spans the range 4.8 to 5.5 over the frequency sweep. The slipping contact ratio peaks at the first resonant mode. At higher drive strain (c), the coordination number decreases at resonance frequency. The slipping contact ratio shows a moderate peak at resonance, than decreases after reaching 20% of mobilised contacts. Results in (b) and (c) show lasting changes in the grain arrangement (coordination number), and dynamic changes in the sample (slipping contact ratio).

Fig. 8 reports the average coordination number at resonance for different loading stresses and local strains. In all cases, the average is constant at low strain and decreases at high strain. High loading stresses reach higher local strain values and we therefore use the sample at $\sigma = 695$ kPa to study the behavior of the system. Variations in initial coordination number (value at low strain) are due to randomness in the packing generation.

In order to test the effect of slipping contacts on the softening, the resonant frequencies of the sample at $\sigma = 695$ kPa are reported for different values of the friction μ_s in Fig. 9(a). The linear and nonlinear regime are identical whether contacts can slip ($\mu_s = 0.22$) and almost not ($\mu_s = 50$ and $\mu_s = 1000$). Fig. 9(b) shows the coordination number for the three friction coefficients. The linear regime spans the same range of strain, and all three systems show a decrease of coordination number in the nonlinear regime. We remark that for this study the different specimens are prepared with the same particle friction $\mu_s = 0.22$ and as a result they show the same initial packing and coordination number. We also studied samples prepared with different initial particle friction and found that the initial coordination number decreases with increasing initial friction coefficient (results not reported here). However, these different packings show the same softening behavior. In the case of high friction, curves in Fig. 9 (a) and (b) have a similar shape. Fig. 9 (c) shows the scaled slipping contact ratio $\mu_s\langle SCR\rangle$ defined as the slipping contact ratio multiplied by the friction coefficient. We found that all scaled data collapses onto a single line showing a linear relation between scaled $\langle SCR\rangle$ and local strain. This means that $\langle SCR\rangle$ is proportional to the friction coefficient both in the linear and nonlinear regime. The tangential component of the interaction force has no or limited impact on the material softening, in contrast with the previous experimental observations where the microslip between the solid beads leads to the softening of contact stiffness and consequently the effective material softening ([9]).

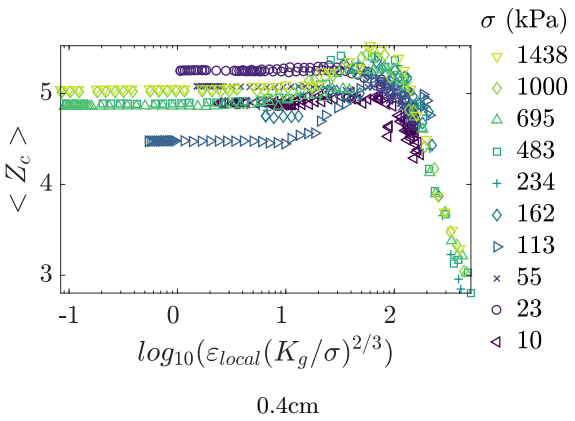

FIG. 8. Coordination number at resonance for the first mode of the different packings. In all cases the coordination number is constant at low strain and decreases at high strains.

CONCLUDING REMARKS

We form granular systems, subject to a normal Hertzian force and a tangential elasto-frictional force, in mechanical equilibrium at a sequence of confining stresses $\sigma = K\varepsilon_0$, where K is the effective bulk modulus of granular samples (Fig. 2) and $10^{-5} \leq \varepsilon_0 \leq 2 \times 10^{-3}$. The bulk modulus of these granular systems K scales with the confining stress as $K \propto \sigma^{0.379}$, close to Hertz theory prediction. The shear modulus G scales as $\sigma^{0.233}$. This scaling is lower than the one found in other published simulations of confined packings [5, 22, 35] and remains open for further analysis.

We subject these granular systems to dynamic testing using AC drive with amplitude A at frequency ω. The output of this dynamic testing at $10^{-7} \leq \varepsilon_{drive} \leq 2 \times 10^{-3}$ is the resonance frequency ω and the local AC strain ε_{local} as a function of A or ε_{drive}. We find to good approximation that the scaled resonance frequency is a universal function of the scaled strain, with the scaling appropriate to a Hertz contact system, $\omega \propto \sigma^{1/6}$, despite of important nonaffine motion of the particles with mean-square displacement being smaller than the particle size.

At low drive amplitudes, $\varepsilon_{drive} < 10^{-4}$, the dynamic response is linear and the effective elastic constant deduced from the resonance frequency is independent of A. At high drive strain $\varepsilon_{drive} \sim 10^{-3}$ being close the static strain by the (high) confining stress, there are large departures from linearity. There the resonance frequency decreases as drive amplitude increases. These departures are taken to represent a reduction in dynamic modulus, termed 'softening'. The softening is a manifestation of the path toward unjamming transition; one infers that at slightly larger drive levels, the material will fluidize. The Hertz scaling extends into the AC amplitude domain in which we observe this softening. Throughout our exploration over (S,A)-space (to be detailed elsewhere), we

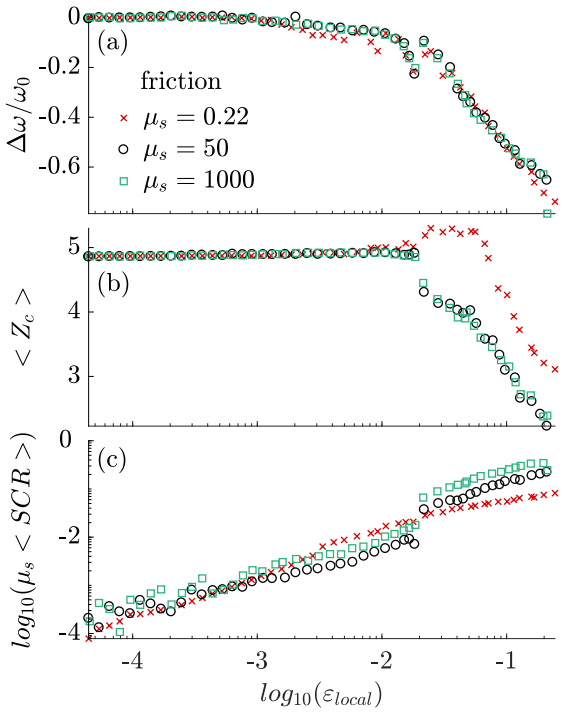

FIG. 9. (a) resonant frequency of sample at $\sigma = 695$ kPa for a range of local strains and three friction coefficients μ_s. μ_s has no impact on the softening or the transition from linear to nonlinear. (b) Coordination number $\langle Z_c \rangle$ and (c) slipping contact ratio multiplied by the friction coefficient $\mu_s \langle SCR \rangle$ at resonance. The behavior of $\langle Z_c \rangle$ is similar and, at high friction, closely follows the shift in resonant frequency of (a). $\langle SCR \rangle$ is proportional to the local strain and to the friction coefficient both in the linear and nonlinear regime.

monitor a number of quantities that could shed light on the microscopic properties of the system, e.g., the average coordination number $\langle Z_c \rangle$, the slipping contact ration $\langle SCR \rangle$ and the average particle velocity v_p.

It is natural to ask if the slipping contact plays a role on the observed elastic softening. We repeated a number of calculations, primarily at $\sigma = 695$ kPa, with the friction coefficient that controls 'slipping' set to values that include almost no slipping, and examined the slipping contact ratio. Even when the number of slipping contacts is reduced by several orders of magnitude we find no significant change in the nonlinear elastic response. The motion afforded by slipping contacts is not the responsible mechanism that contributes to the softening, as found in the experimental observations at strain amplitude of 10^{-6} due to the nonlinear tangential Mindlin contact [7, 9]. Such contact softening mechanism is absent in the present numerical model, but our finding suggests another mechanism of softening likely related to the decrease of the coordination number due to the rearrangement of the particle position, driven by the applied AC amplitude in a manner similar to effective temperature characterized by non-affine motion of the particles [29]. The results are different from those found in 2D simulations where the particle positions are little changed under AC drive [28]. The modulus reduction would be proportional to the amplitude of particle rearrangements which in turn is proportional to the amplitude of the AC drive. The modulus reduction is associated with increased fragility ultimately leading to fluidization, a phase transition not explored here.

In summary we have applied DEM to study the behavior of a particle ensemble, driven progressively harder under resonance conditions. We have done this at several applied loads. We find a material softening manifested by the resonance frequency decrease with AC amplitude. The coordination number is the most telling characteristic measured, showing the softening arises from the breaking and remake of contacts that are brought into existence and given mobility of the particles by the AC drive amplitude. This approach could be valuably applied to the transition from the solid to the fluid states, which is approached in these simulations.

ACKNOWLEDGEMENTS

Paul Johnson and Robert Guyer gratefully acknowledge the US Department of Energy Office of Basic Energy Science and support from EMPA.

* laure.lemrich@alumni.epfl.ch

[1] A. J. Liu and S. R. Nagel, Nature **396**, 21 (1998).
[2] J. Goddard, Proc. R. Soc. London **430**, 105 (1990).
[3] C.-h. Liu and S. R. Nagel, Phys. Rev. B **48**, 15646 (1993).
[4] X. Jia, C. Caroli, and B. Velicky, Phys. Rev. Lett. **82**, 1863 (1999).
[5] H. A. Makse, N. Gland, D. L. Johnson, and L. Schwartz, Phys. Rev. E **70**, 061302 (2004).
[6] A. Norris and D. Johnson, J. Appl. Mech.-T. ASME **64**, 39 (1997).
[7] P. A. Johnson and X. Jia, Nature **437**, 871 (2005).
[8] T. Brunet, X. Jia and P. Johnson, Geophys. Res. Lett. **35**, L19308 (2008).
[9] X. Jia, T. Brunet, and J. Laurent, Phys. Rev. E **84**, 020301 (2011).
[10] P. A. Johnson, B. Zinszner, and P. N. Rasolofosaon, J. Geophys. Res. **101**, 11 (1996).
[11] R. A. Guyer and P. A. Johnson, Phys. Today **52**, 30 (1999).
[12] E. Smith and J. A. Ten Cate, Geophys. Res. Lett. **27**, 1985 (2000).
[13] L. Ostrovsky and P. Johnson, Riv. Nuovo Cimento **24**, 1 (2001).
[14] J. A. TenCate, D. Pasqualini, S. Habib, K. Heitmann, D. Higdon, and P. A. Johnson, Phys. Rev. Lett. **93**, 065501 (2004).

[15] D. Johnson, L. Schwartz, D. Elata, J. Berryman, B. Hornby, and A. Norris, J. Appl. Mech. **65**, 380 (1998).
[16] Y. Khidas and X. Jia, Phys. Rev. E **81**, 021303 (2010).
[17] M.E. Cates, J.P. Wittmer, J.P. Bouchaud, and P. Claudin, Phys. Rev. Lett. **81**, 1841 (1998).
[18] C. Goldenberg and I. Goldhirsch, Nature **435**, 188 (2005).
[19] P. Digby, J. Appl. Mech. **48**, 803 (1981).
[20] K. Walton, J. Mech. Phys. Solids **35**, 213 (1987).
[21] H. A. Makse, N. Gland, D. L. Johnson, and L. M. Schwartz, Phys. Rev. Lett. **83**, 5070 (1999).
[22] C. S. O'Hern, L. E. Silbert, A. J. Liu, and S. R. Nagel, Phys. Rev. E. **68**, 011306 (2003)011306 (2003) .
[23] O. Mouraille, W. Mulder, and S. Luding, J. Stat. Mech. , P07023 (2005).
[24] M. Wyart, L. E. Silbert, S. R. Nagel, and T. A. Witten, Phys. Rev. E **72**, 051306 (2005).
[25] E. Somfai, J.-N. Roux, J. H. Snoeijer, M. van Hecke, and W. van Saarloos, Phys. Rev. E **72**, 021301 (2005).
[26] V. Vitelli, N. Xu, M. Wyart, A. J. Liu, and S. R. Nagel, Phys. Rev. E **81**, 021301 (2010).
[27] N. Xu, V. Vitelli, A. Liu, and S. Nagel, Europhys. Lett. **90**, 56001 (2010).
[28] C.J. Olson Reichhardt, L. Lopatina, X. Jia, and P.A. Johnson, Phys. Rev. E **92**, 022203 (2015).
[29] G. D'Anna and G. Grémaud, Nature **413**, 407 (2001).
[30] S. Van den Wildenberg, M. van Hecke, and X. Jia, Europhys. Lett. **101**, 14004 (2013).
[31] P. A. Cundall and O. D. Strack, geotechnique **29**, 47 (1979).
[32] C. Kloss and C. Goniva, Supplemental Proceedings: Materials Fabrication, Properties, Characterization, and Modeling, Volume 2 , 781 (2011).
[33] K.L. Johnson, Contact mechanics , 84 (1985).
[34] C. Goniva, C. Kloss, N. G. Deen, J. A. Kuipers, and S. Pirker, Particuology **10**, 582 (2012).
[35] I. Agnolin and J.-N. Roux, Phys. Rev. E **76**, 061304 (2007).
[36] I. Agnolin and J.-N. Roux, Phys. Rev. E **76**, 061302 (2007).